

Soham S. Mujumdar

Department of Mechanical Science
and Engineering,
University of Illinois at Urbana-Champaign,
Urbana, IL 61801
e-mail: mujumda2@illinois.edu

Davide Curreli

Assistant Professor
Department of Nuclear,
Plasma, and Radiological Engineering,
University of Illinois at Urbana-Champaign,
Urbana, IL 61801
e-mail: dcurreli@illinois.edu

Shiv G. Kapoor¹

Professor
Department of Mechanical Science
and Engineering,
University of Illinois at Urbana-Champaign,
Urbana, IL 61801
e-mail: sgkapoor@illinois.edu

David Ruzic

Professor
Center for Plasma-Material Interactions,
Department of Nuclear,
Plasma, and Radiological Engineering,
University of Illinois at Urbana-Champaign,
Urbana, IL 61801
e-mail: druzic@illinois.edu

Modeling of Melt-Pool Formation and Material Removal in Micro-Electrodischarge Machining

This paper presents a micro-electrodischarge machining (EDM) melt-pool model to predict workpiece (anode) material removal from a single discharge micro-EDM process. To model the melt-pool, heat transfer and fluid flow equations are solved in the domain containing dielectric and workpiece material. A level set method is used to identify solid and liquid fractions of the workpiece material when the material is molten by micro-EDM plasma heat flux. The plasma heat flux, plasma pressure and the radius of the plasma bubble have been estimated by a micro-EDM plasma model and serve as inputs to the melt-pool model to predict the volume of material removed from the surface of the workpiece. Experiments are carried out to study the effect of interelectrode voltage and gap distance on the crater size. For interelectrode voltage in the range of 200–300 V and gap distance of 1.2 μm , the model predicts crater diameter in the range of 78–96 μm and maximum crater depth of 8–9 μm for discharge duration of 2 μs . The crater diameter values for most of experimental craters show good agreement with the simulated crater shapes. However, the model over-predicts the crater depths compared to the experiments. [DOI: 10.1115/1.4029446]

Keywords: micro-EDM, melt-pool formation, material removal model

1 Introduction

EDM is one of the most widely used techniques among the non-conventional machining methods, mainly due to its ability to produce complex shapes and geometries irrespective of material hardness. Micro-EDM is an adaptation of the EDM process at microscale in which material is removed in subgrain size range (0.1 μm –10 μm) by using lower discharge energies compared to conventional EDM. However, micro-EDM process is considered less efficient due to its lower material removal rate (MRR) [1]. Many efforts have been made to improve MRR of the micro-EDM process by optimizing the machining parameters. However, since EDM is a very complex and stochastic process involving many physical phenomena such as electrodynamics, electromagnetics, thermodynamics, and hydrodynamics; full-scale parametric studies are often required to improve the efficiency once the process conditions are changed [1–3]. Mathematical modeling of the material removal process in micro-EDM process can prove to be helpful in understanding the physics of the process and provide means to optimize the machining parameters to improve process efficiency.

Several attempts have been made by researchers to estimate the material removal in conventional EDM [2] as well as in micro-EDM [4–7]. In most of the studies, the approach has been to model two-dimensional (2D) temperature distribution in the workpiece material under a known heat flux from the plasma. While it is believed that melting and partial evaporation are the

predominant modes of material removal in both cathode and anode, most of the modeling studies consider the material to be a solid body and do not account for hydrodynamic effects. In micro-EDM, the electrical power is dissipated as a plasma discharge in the interelectrode gap filled with dielectric fluid, thereby, forming a molten pool on cathode and anode surfaces. Portion of this melt-pool is ejected as debris at the end of the discharge. However, the influence of hydrodynamic forces on the formation and structure of the melt-pool has rarely been discussed in the context of EDM. Tao et al. [8] made one of the first successful attempts of modeling the melt-pool formation including the effects of the plasma bubble collapse and subsequent solidification. The resulting crater geometries from this model have shown good agreement with the experimental data, however, the crater depths have been over-estimated. While the radius of the plasma and heat flux to the anode have been estimated by empirical relationships with the input machining conditions, the choice for the initial plasma pressure has been somewhat arbitrary.

The aim of this research is to develop a melt-pool model of the micro-EDM discharge based on plasma radius, heat flux, and pressure inputs from the micro-EDM plasma model developed by the authors [9]. The model can be used to simulate melt-pool formation, movement of material by hydrodynamic forces, and predict subsequent material removal in a workpiece with a positive polarity (anode). To model the dynamics of the melt-pool, heat transfer, and fluid flow equations are solved together in the domain containing dielectric and the workpiece. Due to its wide usage, water is considered as the dielectric medium, while Titanium (Alloy 90Ti–6Al–4V) is taken as the workpiece material.

The rest of the paper is divided into six sections. In Sec. 2, the modeling approach used to describe the micro-EDM melt-pool is discussed. Section 3 describes the experimental methodology.

¹Corresponding author.

Contributed by the Manufacturing Engineering Division of ASME for publication in the JOURNAL OF MANUFACTURING SCIENCE AND ENGINEERING. Manuscript received August 8, 2014; final manuscript received December 18, 2014; published online February 23, 2015. Assoc. Editor: Y. B. Guo.

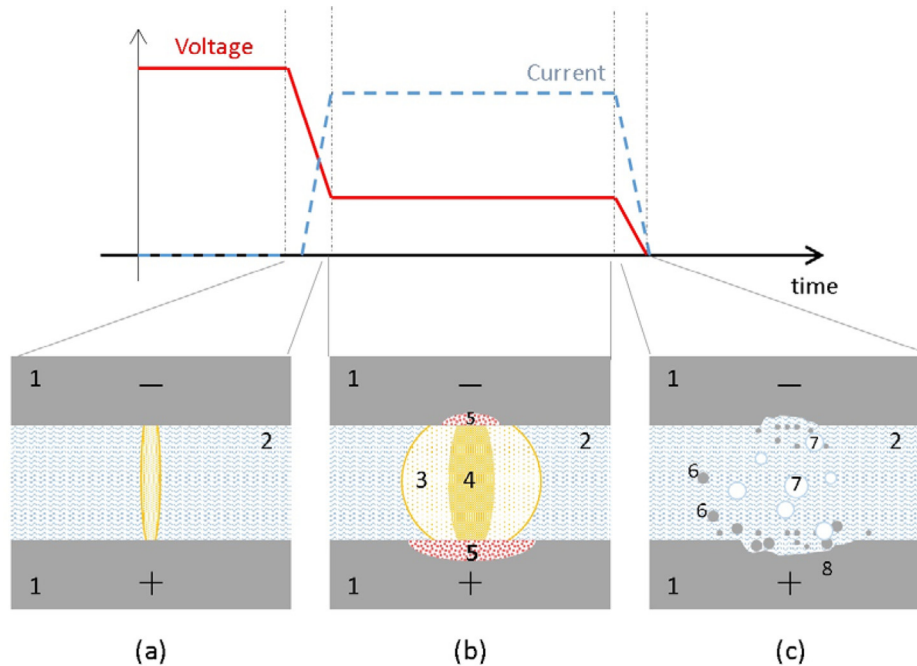


Fig. 1 Schematic of a single discharge of micro-EDM process [9] along with voltage and current conditions showing three main stages: (a) dielectric breakdown stage, (b) discharge stage, and (c) postdischarge stage ((1) electrodes, (2) dielectric, (3) vapor bubble, (4) plasma discharge column, (5) melt-pool, (6) debris, (7) bubbles, and (8) crater)

Section 4 presents the melt-pool simulation for a typical micro-EDM discharge. Experimental validation of the model is presented in Sec. 5. Finally, the conclusions are presented in Sec. 6.

2 Model Formulation

Basic stages of a single micro-EDM discharge are shown in Fig. 1. In micro-EDM, the tool (cathode) and workpiece (anode) are separated by a gap distance of the order $1\text{--}10\text{ }\mu\text{m}$ filled with dielectric fluid. A discharge is then made by applying a voltage between the electrodes for a small duration of time. The high intensity electric field generated by the applied voltage in a small gap breaks down the dielectric medium causing the current to rise and form a plasma channel in the gap. The plasma channel expands radially, while heating the workpiece and tool electrode surfaces. At the end of the discharge, the plasma channel collapses causing implosion of the dielectric fluid and splashing of the melt-pool, leaving behind small craters on the electrode surface [7].

Due to complexities involving micro-EDM plasma, dielectric medium, melt-pool formation at both tool and workpiece electrodes, plasma collapse, and flushing of the dielectric etc., the heat flux, pressure, and radius of the plasma are obtained separately by simulating a micro-EDM model [9] and thereafter, the melt-pool formation due to a single discharge micro-EDM event is modeled based on the outputs of the plasma model. As shown in Fig. 2, plasma heat flux and pressure from the plasma model are imposed on the workpiece surface to model the temperature distribution and flow of the melt-pool. Furthermore, following assumptions have been made to simplify the model. These assumptions are adapted from the literature on the micro-EDM modeling [2,7,10] and the weld-pool modeling [11,12].

- (1) Workpiece and tool material are homogeneous and isotropic.
- (2) Thermophysical properties of the workpiece material do not vary with temperature except at the phase change. Thermophysical properties of the dielectric material are assumed to be constant with temperature.
- (3) Liquid phase of the workpiece material and dielectric fluid are incompressible and the flow in the melt-pool is laminar.

(4) Vaporization of the dielectric and the workpiece material is neglected.

(5) After the discharge, it is assumed that 100% of the molten material is removed from the workpiece surface [4,5,7]. In actual process, the molten material is ejected due to plasma implosion at the end of the discharge. Therefore, some of the material may resolidify in and around the crater.

The formulation of the model for micro-EDM melt-pool is discussed further in detail in remainder of this section. A brief discussion of the global micro-EDM plasma discharge model that provides the plasma heat flux, pressure and plasma radius inputs to the melt-pool model is given in Sec. 2.1. Governing equations involved in the micro-EDM melt-pool model, namely, level-set equation, fluid flow equations and heat transfer equation, are presented in Sec. 2.2. Finally, Sec. 2.3 describes geometry and the boundary conditions.

2.1 Micro-EDM Plasma Model. To model micro-EDM plasma, the global plasma model approach [9,13,14] is used, which assumes uniform spatial distributions of plasma characteristics and

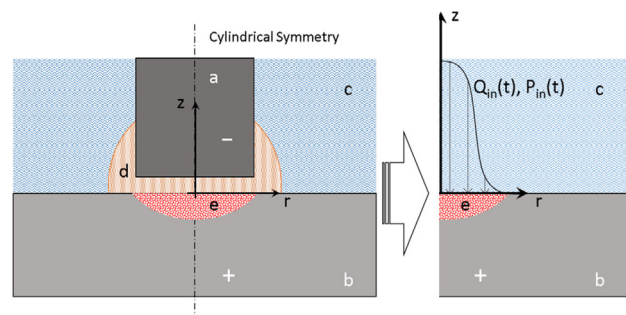


Fig. 2 Schematic of the micro-EDM melt-pool modeling domain, (a) tool electrode (cathode), (b) workpiece electrode (anode), (c) dielectric fluid, (d) plasma channel, and (e) melt-pool at the workpiece surface

involves simple governing equations of conservation of mass and energy to estimate first-hand estimates of the time-transients. Figure 3 shows basic schematic of the plasma model [9], which consists of three submodules, namely, plasma chemistry that solves the reaction kinetics involving ionization, dissociation, and recombination reactions; power balance that solves for the temperature of the plasma; and bubble dynamics module that gives the evolution of plasma geometry during the discharge. More details of the model are provided elsewhere [9].

Electrical voltage and power going into the micro-EDM plasma measured during the experiments serve as the inputs to the plasma model along with the interelectrode gap distance. Since the model assumes spatially uniform plasma characteristics in the plasma bubble, Gaussian functions in space are imposed onto the values of heat flux and pressure predicted by the model to mimic spatial variation of these quantities

$$Q_{in}(r, t) = Q_0(t)F(r), \quad 0 \leq r \leq R(t) \quad (1)$$

and

$$P(r, z, t) = P_0(t)G(r, z), \quad 0 \leq r \leq R(t), 0 \leq z \leq L \quad (2)$$

where, $Q_0(t)$ (W/m²) and $P_0(t)$ (N/m²) are the time-dependent values of heat flux and plasma pressure predicted by the plasma model [9], respectively. $R(t)$ (m) is the radius of the plasma bubble predicted by the model and L (m) is the interelectrode gap distance. $F(r)$ is the Gaussian function imposed on the heat flux in radial direction and $G(r, z)$ is the Gaussian function imposed on the pressure in radial and axial directions

$$F(r) = \frac{R(t)^2}{2\sigma_R^2 \left[1 - \exp\left(-\frac{R(t)^2}{\sigma_R^2}\right) \right]} \exp\left[-\frac{r^2}{2\sigma_R^2}\right] \quad (3)$$

and

$$G(r, z) = \exp\left[-\frac{r^2}{2\sigma_R^2}\right] \exp\left[-\frac{(z - L/2)^2}{2\sigma_z^2}\right] \quad (4)$$

with parameters σ_R and σ_z suitably chosen as

$$\sigma_R = R_e/3 \quad (5)$$

$$\sigma_z = L/3 \quad (6)$$

where R_e (m) is the tool electrode (cathode) radius.

2.2 Governing Equations of the Melt-Pool model. Due to intense heat generated by the plasma during the micro-EDM process, workpiece material is in molten state during the discharge.

Therefore, differential equations governing hydrodynamic flow and heat transfer need to be solved together in the domain. Also, due to advection and convection effects in the melt-pool, workpiece surface undergoes deformations that can not be neglected. Therefore, the physics governing the tracking of the workpiece surface due to the deformations is also included in this model.

2.2.1 Workpiece Surface Tracking. In order to model the surface tracking, the level set method is applied [15]. A function $\phi(r, z, t)$ is defined over the entire domain to describe the interface according to the following criteria:

$$\phi(r, z, t) \begin{cases} < 0.5, & \text{dielectric;} \\ = 0.5, & \text{interface;} \\ > 0.5, & \text{workpiece} \end{cases} \quad (7)$$

Due to function ϕ that is defined everywhere in the domain, it is possible to transform the domain into a continuum where any physical property f such as density (ρ), viscosity (η), etc. can be defined at each point (r, z) in the domain as

$$f = f_{\text{dielectric}} + (f_{\text{workpiece}} - f_{\text{dielectric}})\phi \quad (8)$$

The movement of the surface is then described by a differential equation, which is solved together with Navier–Stokes and heat-transfer equations [15]

$$\frac{\partial \phi}{\partial t} + \mathbf{u} \cdot \nabla \phi = \gamma_{ls} \nabla \cdot \left(\epsilon_{ls} ((\nabla \phi \cdot \mathbf{n})) - \phi(1 - \phi) \frac{\nabla \phi}{|\nabla \phi|} \right) \quad (9)$$

Here, \mathbf{u} (m/s) is the velocity vector, ϵ_{ls} is the interface thickness that is generally set to half of the maximum mesh element size in the domain. The term γ_{ls} is the stabilization parameter that determines the repetition of the re-initialization for each time step. The γ_{ls} is suitably set to 11. The interface normal vector, \mathbf{n} , is defined by

$$\mathbf{n} = \frac{\nabla \phi}{|\nabla \phi|} \Big|_{\phi=0.5} \quad (10)$$

Based on \mathbf{n} , curvature of the free surface, i.e., the interface between the dielectric and the workpiece, can be found out as

$$\kappa_S = -\nabla \mathbf{n} \Big|_{\phi=0.5} \quad (11)$$

Surface curvature, κ_S (1/m), is essential in implementing the surface tension force. However, as the interface is changing over time, it is necessary to transform surface forces such as surface tension and plasma pressure into volumetric forces using a smoothed, continuously differentiable delta function [15]

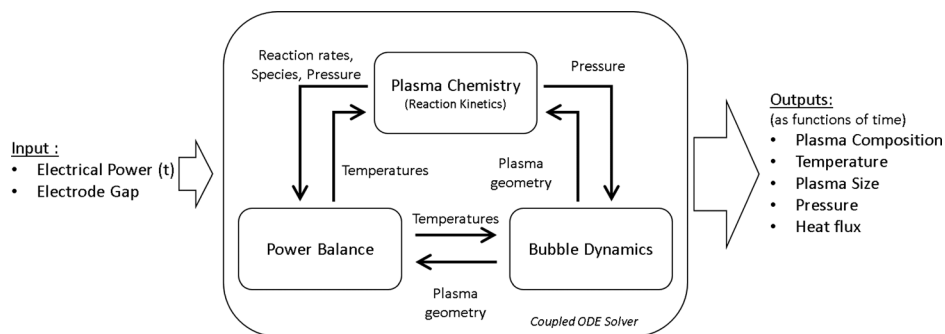


Fig. 3 Schematic of the micro-EDM plasma model algorithm [9]

$$\delta = 6|\nabla\phi||\phi(1-\phi)| \quad (12)$$

2.2.2 Heat Transfer. The heat transfer in the entire domain can be described using differential equation

$$\rho c_p \frac{\partial T}{\partial t} + \rho c_p \mathbf{u} \cdot \nabla T = \nabla \cdot (k \nabla T) + Q_{in} \delta \quad (13)$$

where ρ (kg/m³) is the density, c_p (J/(kg K)) is the specific heat capacity, T (K) is the temperature, k (W/(m K)) is the thermal conductivity, and Q_{in} (W/m²) represents the incoming heat flux from the plasma to the workpiece surface given by Eq. (1).

In order to model the phase change of workpiece material from solid to liquid, a smoothed Heaviside function, $H(T)$, is used to represent volume fraction of the liquid phase, g_l , at each grid point in the domain. δT_m is the width of the temperature region (Mushy Zone) in which $H(T, \delta T_m)$ changes from 0 to 1 and is assumed to be 50 K [11]. This allows us to define the workpiece material as a continuum (see Fig. 4), where thermophysical properties of the material are defined as

$$f(T) = f_{sol} - (f_{sol} + f_{liq})g_l \quad (14)$$

$$\text{with, } g_l = H(T) = \frac{1}{2} + \frac{1}{2} \text{erf}\left(\frac{T - T_m}{10}\right) \quad (15)$$

To account for change in the enthalpy of the material in going from solid phase to liquid phase, specific heat capacity (C_p) is formulated as

$$C_p = C_s g_s + C_l g_l + H_f \frac{d}{dT}(H(T)) \quad (16)$$

where C_s (J/(kg K)) is the specific heat capacity of the solid phase, C_l (J/(kg K)) is the specific heat capacity of the liquid phase, T_s (K) is the solidus temperature, T_l (K) is the liquidus temperature, H_f (J/kg) is the latent heat of fusion, and $H(T)$ is the smoothed Heaviside function given in Eq. (15).

2.2.3 Hydrodynamics. Assuming the melt-pool is an incompressible fluid, the fluid motion in the melt-pool can be described using Navier–Stokes equation and the equation of continuity as

$$\rho \frac{\partial \mathbf{u}}{\partial t} + \rho(\mathbf{u} \cdot \nabla) \mathbf{u} = \nabla \cdot [-p \mathbf{I} + \mu(\nabla \mathbf{u} + (\nabla \mathbf{u})^T)] + \mathbf{F}_{sur} + \mathbf{F}_m \quad (17)$$

$$\nabla \cdot \mathbf{u} = 0 \quad (18)$$

where p (Pa) is the pressure and \mathbf{I} is the identity tensor.

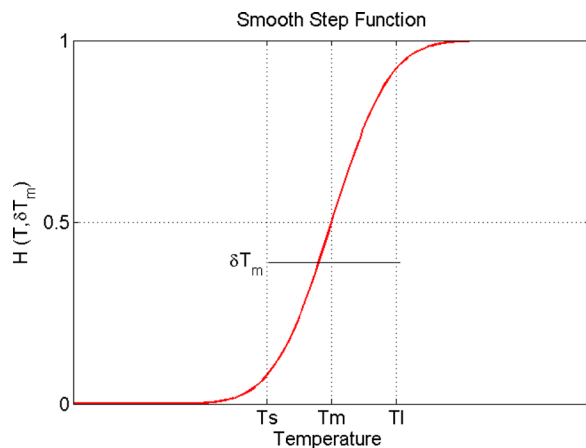


Fig. 4 Smoothed Heaviside step function

The force term \mathbf{F}_{sur} contains surface tension force, the Marangoni force and the force exerted by plasma pressure

$$\mathbf{F}_{sur} = \left[2\gamma\kappa_S \mathbf{n} - \frac{\partial\gamma}{\partial T}(\mathbf{I} - \mathbf{nn}) \cdot \nabla T - P\mathbf{n} \right] \delta \quad (19)$$

where γ (N/m) is the surface tension of liquid phase of workpiece material, specified as a function of temperature. The surface forces are multiplied by δ to convert them into volumetric forces and make sure that they appear only at the interface between dielectric and workpiece. Plasma pressure, P is given by Eq. (2).

In order to impart zero velocities in the solid region, an artificial damping force \mathbf{F}_m is introduced in the Navier–Stokes equations [11]

$$\mathbf{F}_m = \frac{\mu}{K} \frac{\rho}{\rho_l} \mathbf{u} \quad (20)$$

Here a permeability function K analogous to fluid flow in porous media is assumed employing the Carman–Kozeny equation [11]

$$K = \frac{g_l^3}{c_1(1 - g_l)^2}, \quad c_1 = \frac{180}{d^2} \quad (21)$$

where d is proportional to dendrite dimension, which is assumed to be 10^{-2} cm [11].

2.3 Geometry and Boundary Conditions. To model the melt flow, a 2D axisymmetric domain is considered as shown in Fig. 5. A cylindrical coordinate system was placed at the center of the initial free surface of the workpiece. The domain was meshed with free triangular elements with denser mesh density near the initial dielectric-workpiece interface. The boundary conditions used are given in Table 1. The model was solved with COMSOL 4.3a Multiphysics® software. PARDISO solver was used with double precision settings and automatic time-stepping to solve coupled energy-momentum equations.

3 Micro-EDM Experiments

Single discharge experiments were carried out on a customized micro-EDM setup consisting of a hybrid RC-transistor-based circuit [16] to generate a single DC voltage pulse of specific amplitude and pulse width for each trial. A 100 μ m diameter tungsten rod was used as Tool electrode with negative polarity (cathode), while grade-5 titanium alloy (90Ti–6Al–4V) was used as the workpiece (anode). De-ionized (DI) water was used as dielectric liquid. Open gap voltage (V_0) and the interelectrode gap distance (L) were chosen as two process parameters to make a full-factorial experimental design using 3 levels of voltage and 2 levels of gap

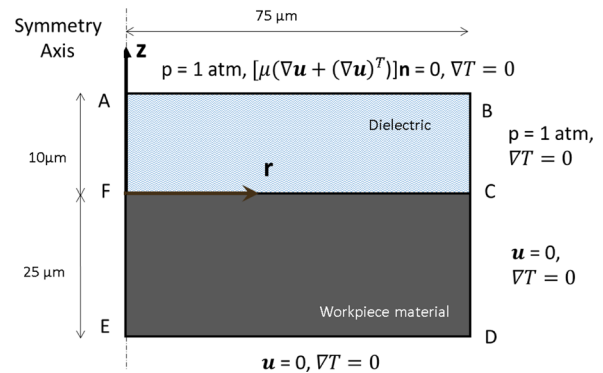


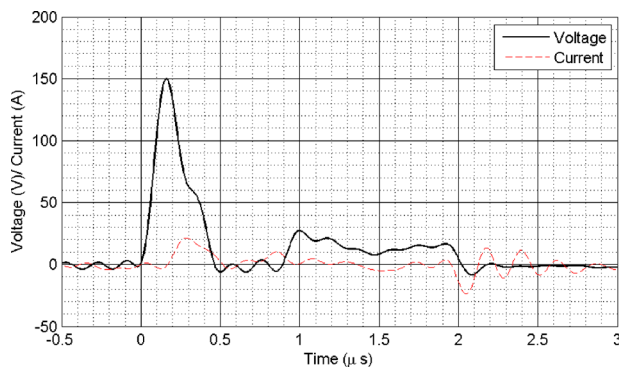
Fig. 5 Modeling domain with boundary condition

Table 1 Boundary conditions for numerical calculations

Boundary (see Fig. 5)	Navier–Stokes equation	Heat transfer equation
AE	Symmetry	Symmetry
CD, DE	No slip ($\mathbf{u} = 0$)	Adiabatic wall ($\nabla T = 0$)
AB	Pressure inlet, no viscous stress ($p = 1$ atm, $[\mu(\nabla \mathbf{u} + (\nabla \mathbf{u})^T)] \cdot \mathbf{n} = 0$)	Adiabatic wall ($\nabla T = 0$)
BC	Pressure outlet ($p = 1$ atm)	Adiabatic wall ($\nabla T = 0$)

Table 2 Levels of voltage (V_0) and gap (L) used for the experiments

Process parameter	Unit	Levels
Open gap voltage (V_0)	V	200, 250, 300
Gap distance (L)	μm	1, 2

**Fig. 6 Typical micro-EDM discharge waveform ($V_0 = 200$ V, $L = 2$ μm)**

as shown in Table 2. For each combination of voltage and gap, five repetitions were carried out.

Voltage and current data for the discharge was collected during each trial using a 2 GigaSamples/s Tektronix TDS2024B

oscilloscope. A typical voltage and current waveform of micro-EDM discharge is shown in Fig. 6. The voltage across the electrode gap is at open gap voltage at the beginning of the discharge and the current is zero due to the dielectric present in the gap that acts as an insulator. But as the electric field intensity reaches the dielectric strength of the dielectric material, dielectric breaks down, and discharge plasma is formed in the gap allowing a current to flow from the anode to the cathode. The voltage measured across the electrodes drops as the current flows in the gap as seen in Fig. 6. Instantaneous power ($P_0(t)$) was obtained by taking product of instantaneous voltage ($V(t)$) and current ($I(t)$) to be used as an input for the micro-EDM plasma model.

4 Micro-EDM Melt-Pool Simulation

The melt-pool model described in Sec. 2 was simulated to obtain evolution the melt-pool and crater formation. The heat flux, pressure, and radius of the plasma required for the melt-pool model were obtained from the micro-EDM plasma model [9] for given discharge conditions. Thermophysical properties of the workpiece material (Grade 5 Titanium) and the dielectric liquid (DI water) used in the melt-pool simulation are shown in Table 3.

Figure 7 presents the evolution of the melt-pool in the workpiece material and corresponding velocity distribution of the melt-pool for interelectrode voltage of 200 V and gap distance of 2 μm . Initially, at $t = 0$ the material in the domain is assumed to be at uniform ambient temperature. As the time progresses, the heat flux from the plasma heats the workpiece surface converting a part of it into liquid forming a melt-pool. The surface of the melt-pool is acted upon by the hydrodynamic forces such as plasma pressure and surface tension. For the pressure values predicted by the plasma model, it is seen that the pressure force is the most dominant force, which deforms the top surface of the melt-pool. As seen in Fig. 7, as more and more heat flux is supplied to the workpiece surface, temperature at the center of the melt-pool rises and the heat is conducted in radial and axial direction away from the center. Also, the radius of the plasma bubble grows in size as the discharge progresses, effectively bringing more area of the workpiece surface under influence of the plasma heat flux and pressure. Therefore, the size of the melt-pool grows in radial (r) as well as in axial (z) direction as depicted by the white contour line plotted in Figs. 7(a), 7(c), 7(e), and 7(g) at each time step of 0.5 μs during the discharge duration of 2 μs . The diameter of the melt-pool is 38 μm at $t = 0.5$ μs , which grows to 78 μm at the end

Table 3 Thermophysical properties

Property	Symbol	Value	Unit
<i>Titanium alloy (90Ti–6Al–4V) [15,17]</i>			
Density of solid phase	ρ_s	4520	kg m^{-3}
Density of liquid phase	ρ_l	4110	kg m^{-3}
Thermal conductivity of solid phase	k_s	30	$\text{W m}^{-1} \text{K}^{-1}$
Thermal conductivity of liquid phase	k_l	21	$\text{W m}^{-1} \text{K}^{-1}$
Specific heat of solid phase	c_s	610	$\text{J kg}^{-1} \text{K}^{-1}$
Specific heat of liquid phase	c_l	700	$\text{J kg}^{-1} \text{K}^{-1}$
Thermal expansion coefficient	β_T	8×10^{-6}	K^{-1}
Melting point	T_m	1903	K
Solidus temperature	T_s	1878	K
Liquidus temperature	T_l	1928	K
Width of the temperature region in mushy zone	δT_m	50	K
Ambient/Initial temperature	T_a	300	K
Latent heat of fusion	H_f	3.7×10^5	J kg^{-1}
Dynamic viscosity	μ	0.005	$\text{kg m}^{-1} \text{s}^{-1}$
Surface tension	γ	$1.65\text{--}2.4 \times 10^{-4}(T - T_m)$	Nm^{-1}
<i>De-ionized water</i>			
Density	ρ	1000	kg m^{-3}
Thermal conductivity	k	2.18	$\text{W m}^{-1} \text{K}^{-1}$
Specific heat	c_s	4200	$\text{J kg}^{-1} \text{K}^{-1}$
Dynamic viscosity	μ	0.001	$\text{kg m}^{-1} \text{s}^{-1}$

of the discharge duration at $t = 2 \mu\text{s}$. Similarly, the depth of the melt-pool grows from $3.6 \mu\text{m}$ to $8.1 \mu\text{m}$ from $t = 0.5 \mu\text{s}$ to $t = 2 \mu\text{s}$. It is noted that the maximum temperature in the domain predicted by the model is 7769 K occurring at $t = 1.2 \mu\text{s}$, which is higher than what is observed in the actual process [18]. This is because the melt-pool model discussed in this paper neglects the vaporization of the workpiece material and the latent heat of vaporization during the phase change from liquid to vapor. Also, the plasma

model used to estimate the heat flux assumes spatially uniform plasma characteristics. A better estimation of the temperature distribution can be obtained by more accurate plasma model and modeling of vaporization of the workpiece material along with the melt-pool evolution.

The velocities of the melt-flow during the discharge are presented in Figs. 7(b), 7(d), 7(f), and 7(h). The flow of the molten material is mainly dictated by the Marangoni stress, i.e.,

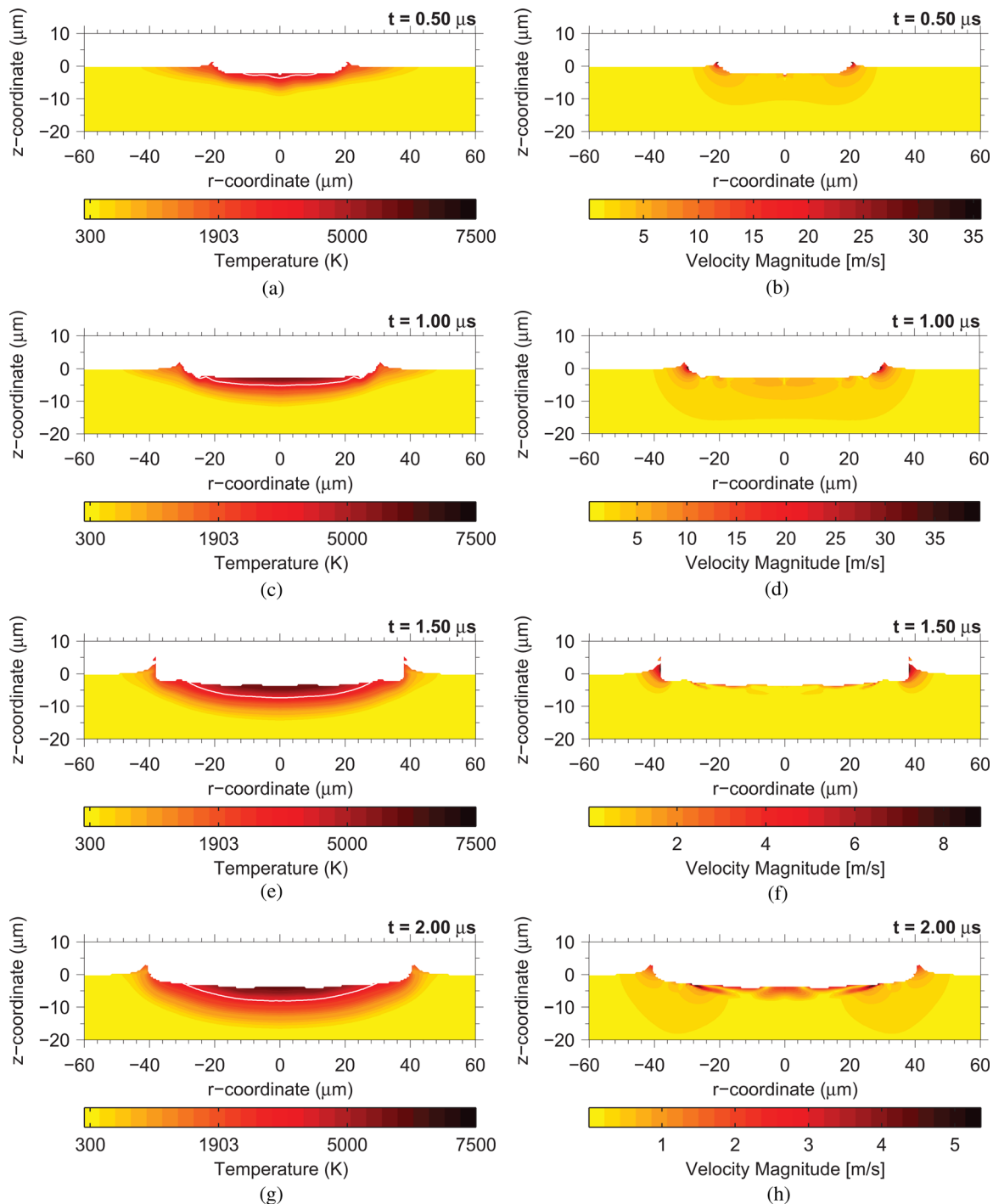


Fig. 7 Evolution of temperature and velocities of the melt-pool in a typical micro-EDM discharge with $V_0 = 200 \text{ V}$, $L = 2 \mu\text{m}$ (shape of the melt-pool is traced by a white contour line). (a) Temperature ($t = 0.5 \mu\text{s}$), (b) melt-pool velocities ($t = 0.5 \mu\text{s}$), (c) temperature ($t = 1 \mu\text{s}$), (d) melt-pool velocities ($t = 1 \mu\text{s}$), (e) temperature ($t = 1.5 \mu\text{s}$), (f) melt-pool velocities ($t = 1.5 \mu\text{s}$), (g) temperature ($t = 2 \mu\text{s}$), and (h) melt-pool velocities ($t = 2 \mu\text{s}$).

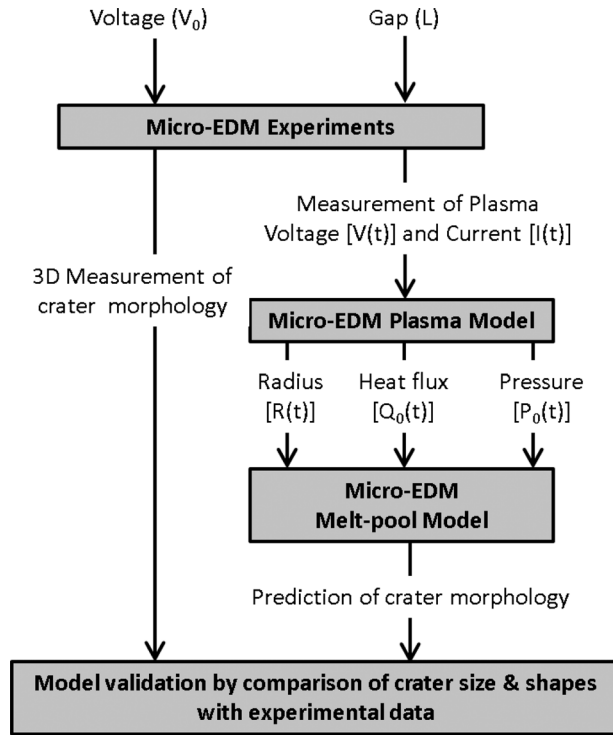


Fig. 8 Approach for melt-pool model validation

temperature-dependent surface tension force, and the plasma pressure. Due to strong temperature gradients in the melt-pool from center toward the edge, a strong Marangoni stress is exerted on the material, pushing the material radially outward from the center. Therefore, the maximum velocities are observed at the edges of the melt-pool as seen from Figs. 7(b), 7(d), and 7(f). The model predicts maximum velocity of 130 m/s in the melt-pool at $t = 0.9 \mu\text{s}$.

5 Experimental Validation

The approach used to validate the micro-EDM melt-pool model is shown in Fig. 8. First, single discharge micro-EDM experiments were designed by varying the process conditions, namely, open gap voltage (V_0) and interelectrode gap distance (L). The plasma voltage and current waveforms measured during each trial were then supplied to the micro-EDM plasma model to obtain temporal description of plasma characteristics such as heat flux to the workpiece ($Q_0(t)$), plasma pressure (P_0) and plasma bubble radius ($R(t)$). Time-averaged values of the results obtained from the plasma model are listed in Table 4. Using these outputs of the plasma model and the numerical model described in Secs. 2.2 and 2.3, melt-flow in a single discharge micro-EDM process is simulated.

5.1 Comparison of Crater Shapes. To find the shapes of the experimental craters, 3D imaging of each discharge crater was

Table 4 Micro-EDM plasma model results showing time-averaged values of heat flux and pressure, and maximum radius

Voltage (V_0)	Gap (μm)	Heat flux (W/m^2)	Pressure (atm)	Radius (μm)
200	1	2.33×10^{10}	328	325
200	2	2.31×10^{10}	196	255
250	1	2.95×10^{10}	290	299
250	2	2.27×10^{10}	227	269
300	1	1.10×10^{10}	307	303
300	2	2.98×10^{10}	230	269

conducted by laser scanning. The Z-axis of a three-axis microscale machine tool (mMT) was fitted with a Keyence LT-9010M surface scanning confocal laser with $0.01 \mu\text{m}$ distance resolution, while the workpiece was affixed to the XY-axes of the mMT to enable raster-scanning of the surface. The laser scans over the surface collecting discrete height measurements moving in steps of $1 \mu\text{m}$. The surface topology was digitally recreated from the data gathered by the laser, by plotting the height data for every point in a matrix with $1 \mu\text{m}$ spacing between the points, as shown in Fig. 9(a).

To estimate the final crater shape from the model, it was assumed that 100% of the molten material is removed from the discharge site due to the collapse of the plasma at the end of the discharge ($t = 2 \mu\text{s}$). Cross-sectional profiles of the experimental craters in two mutually perpendicular directions (X , Y) were averaged and compared with the corresponding crater shape generated by the melt-pool simulation as shown in Fig. 10 for a typical trial with open gap voltage (V_0) of 200 V and interelectrode gap (L) of $2 \mu\text{m}$. Figure 11 presents comparison of cross-sectional profiles of experimental and simulated craters for each discharge condition in terms of crater diameter and crater depth. For all the discharge conditions simulated, the model estimates diameter of the craters in the range of $78\text{--}96 \mu\text{m}$ and maximum crater depth in the range of $8\text{--}9 \mu\text{m}$. Whereas, the crater diameter measured for across all the combinations of voltage and gap lies in the range of $60\text{--}81 \mu\text{m}$ and crater depth in the range of $4\text{--}7 \mu\text{m}$. From Fig. 11(a), it is observed the simulated crater diameter shows reasonable agreement with the experimental crater diameter for all the trials except for $V_0 = 200 \text{ V}$ and $L = 1 \mu\text{m}$. However, Fig. 11(b) shows that the model always predicts greater crater depths when compared to the experiments. The model presented here assumes 100% removal of

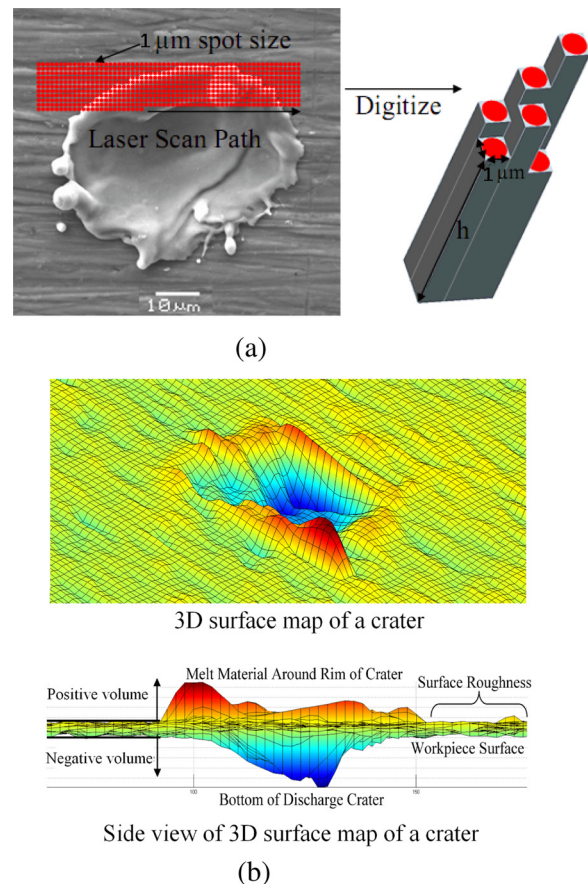


Fig. 9 3D imaging of crater surface with laser scanning [1]: (a) digitizing crater surface with laser scanning and (b) crater surface showing positive and negative volumes

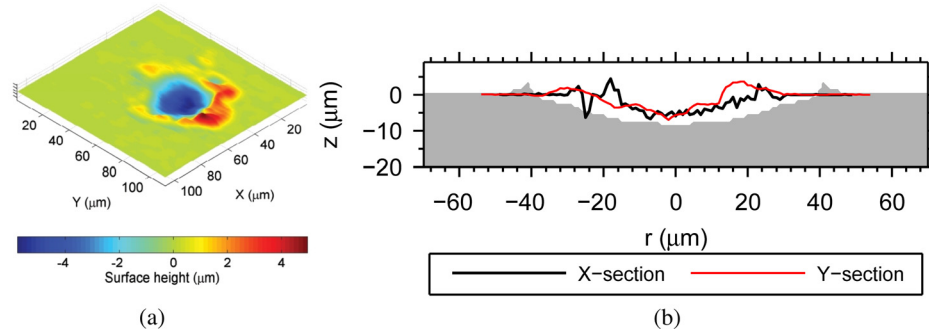


Fig. 10 3D image and cross-sectional profile of a typical discharge crater obtained in experimental trials and its comparison with simulated crater shape ($V_0 = 200$ V, $L = 2$ μm). (a) 3D Image of experimental crater and (b) comparison of predicted crater profile with experimental measurement.

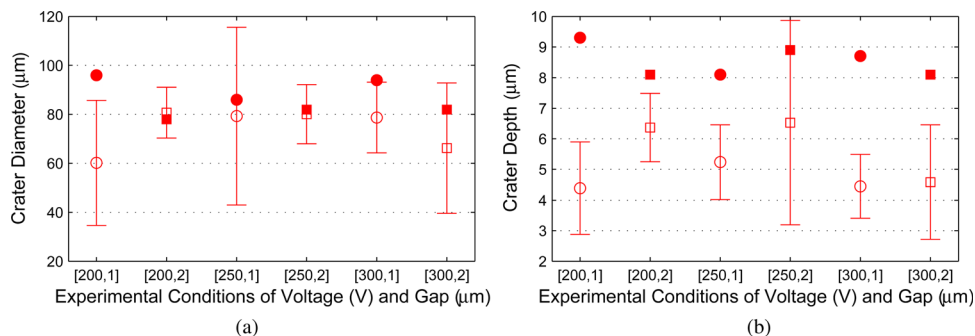


Fig. 11 Comparison of crater profiles between model and the experiments (filled: model predictions, unfilled: experimental mean with error bars at \pm standard deviation). (a) Comparison of crater diameters and (b) comparison of crater depths.

the molten material from the discharge site after the discharge, however, in actual process, the ejection of the molten material away from the discharge site at the end of the discharge is less effective and a fraction of the melt-pool resolidifies at the discharge site itself, leaving behind shallower craters.

6 Conclusions

This paper explains development of a melt-pool model to estimate the material removed in a single discharge of micro-EDM process. The melt-pool was modeled by solving heat transfer and fluid flow equations in the domain containing the dielectric and workpiece materials. To model the flow of liquid metal under hydrodynamic forces such as the plasma pressure and surface tension, level-set method was used to calculate the liquid and solid fractions of the workpiece material in the domain. Using the melt-pool model, the micro-EDM melt-pool formed due to application of micro-EDM plasma heat flux and pressure was simulated to obtain temperature distribution in the workpiece and shape of the resulting crater. Further, experiments were carried out to investigate effect of the interelectrode voltage and gap distance on crater profiles. Same discharge conditions were then simulated using the melt-pool model to compare the experimental results with the simulations. The specific conclusions of the research are noted as follows:

- (1) The micro-EDM melt-pool model is used to predict the temperature distribution and the melt-flow of the workpiece material under influence of micro-EDM plasma heat flux and pressure. Assuming 100% of the molten material is removed after the plasma collapse at the end of the discharge, profiles of the melt-pool was estimated as the profile of the resulting crater.

- (2) Values of the plasma heat flux, pressure and radius are obtained by simulating micro-EDM plasma model [9] for the discharge conditions specified by interelectrode voltage and gap distance.
- (3) The cross-sectional profiles of the craters simulated by the melt-pool model predict the diameter of the discharge crater in the range of 78–96 μm and maximum crater depth in the range of 8–9 μm for discharge duration of 2 μs . It was observed that the diameters of the simulated craters agree reasonably well with the corresponding experimental measurements for almost all the discharge conditions. However, the crater depths measured in the experiments are smaller than the simulated crater depths. This may be due to partial ejection of all the molten material after the discharge and resolidification of some of the material at the discharge site. It is believed that a better match between the model and experiments can be obtained by incorporating the physics of resolidification of material post discharge.

Acknowledgment

This material was based in part upon work supported by the National Science Foundation under Award No. 1033362. The authors are grateful to NSF for funding this research. The authors would also like to thank Dr. Deepak Marla for discussions and his helpful suggestions to the research.

References

- [1] Heinz, K., 2010, "Fundamental Study of Magnetic Field-Assisted Micro-EDM for Non-Magnetic Materials," M.S. thesis, University of Illinois at Urbana-Champaign, Champaign, IL.
- [2] Yeo, S., Kurnia, W., and Tan, P., 2008, "Critical Assessment and Numerical Comparison of Electro-Thermal Models in EDM," *J. Mater. Process. Technol.*, **203**(1–3), pp. 241–251.

- [3] Boothroyd, C., 2006, *Fundamentals of Machining and Machine Tools*, CRC/ Taylor & Francis, Boca Raton, FL.
- [4] Snoeys, R., and Dijck, F. S. V., 1972, "Plasma Channel Diameter Growth Affects Stock Removal in EDM," *CIRP Ann.*, **21**(1), pp. 39–40.
- [5] Patel, M., Barrufet, M., Eubank, P., and Dibitonto, D., 1989, "Theoretical Models of the Electrical Discharge Machining Process II. The Anode Erosion Model," *J. Appl. Phys.*, **66**(9), pp. 4104–4111.
- [6] Singh, A., and Ghosh, A., 1999, "Thermo-Electric Model of Material Removal During Electric Discharge Machining," *Int. J. Mach. Tools Manuf.*, **39**(4), pp. 669–682.
- [7] Joshi, S., and Pande, S., 2010, "Thermo-Physical Modeling of Die-Sinking EDM Process," *J. Manuf. Processes*, **12**(1), pp. 45–56.
- [8] Tao, J., Ni, J., and Shih, A., 2012, "Modeling of the Anode Crater Formation in Electrical Discharge Machining," *ASME J. Manuf. Sci. Eng.*, **134**(1), p. 011002.
- [9] Mujumdar, S. S., Curreli, D., Kapoor, S. G., and Ruzic, D., 2014, "A Model of Micro Electro-Discharge Machining Plasma Discharge in Deionized Water," *ASME J. Manuf. Sci. Eng.*, **136**(3), p. 031011.
- [10] Ikai, T., and Hashigushi, K., 1995, "Heat Input for Crater Formation in EDM," *Proceedings of the International Symposium for Electro-Machining-ISEM XI*, EPFL, pp. 163–170.
- [11] Hu, J., Guo, H., and Tsai, H. L., 2008, "Weld Pool Dynamics and the Formation of Ripples in 3D Gas Metal Arc Welding," *Int. J. Heat Mass Transfer*, **51**(9), pp. 2537–2552.
- [12] Xu, G., Hu, J., and Tsai, H. L., 2012, "Modeling Three-Dimensional Plasma Arc in Gas Tungsten Arc Welding," *ASME J. Manuf. Sci. Eng.*, **134**(3), p. 031001.
- [13] Lieberman, M., and Lichtenberg, A. J., 2005, *Principles of Plasma Discharges and Material Processing*, Wiley, New York.
- [14] Meyyappan, R., and Govindan, T., 1995, "Modeling of Electron Cyclotron Resonance Discharges," *IEEE Trans. Plasma Sci.*, **23**(4), pp. 623–627.
- [15] Hoche, D., Muller, S., Rapin, G., Shinn, M., Remdt, E., Gubisch, M., and Schaaf, P., 2009, "Marangoni Convection During Free Electron Laser Nitriding of Titanium," *Metall. Mater. Trans. B*, **40**(4), pp. 497–507.
- [16] Heinz, K., Kapoor, S. G., DeVor, R. E., and Surla, V., 2011, "An Investigation of Magnetic-Field-Assisted Material Removal in Micro-EDM for Nonmagnetic Materials," *ASME J. Manuf. Sci. Eng.*, **133**(2), p. 021002.
- [17] Rai, R., Elmer, J., Palmer, T., and DebRoy, T., 2007, "Heat Transfer and Fluid Flow During Keyhole Mode Laser Welding of Tantalum, Ti–6Al–4V, 304l Stainless Steel and Vanadium," *J. Phys. D.: Appl. Phys.*, **40**(18), pp. 5753–5766.
- [18] Kunieda, M., Lauwers, B., Rajurkar, K., and Schumacher, B., 2005, "Advancing EDM Through Fundamental Insight Into the Process," *CIRP Ann.*, **54**(2), pp. 67–87.